Oxygen reduction reaction kinetics on a Pt thin layer electrode in AEMFC

(article starts on next page)

Oxygen reduction reaction kinetics on a Pt thin layer electrode in AEMFC

Eva Marra [a],[*], Henrik Grimler [a], Gerard Montserrat-Sisó [b], Rakel Wreland Lindström [a], Björn Wickman [b], Göran Lindbergh [a], Carina Lagergren [a]

[a] Department of Chemical Engineering, KTH Royal Institute of Technology, SE-100 44 Stockholm, Sweden
[b] Department of Physics, Chalmers University of Technology, SE-412 96 Gothenburg, Sweden

ABSTRACT

The study of the catalytic activity in a fuel cell is challenging, as mass transport, gas crossover and the counter electrode are generally interfering. In this study, a Pt electrode consisting of a thin film deposited on the gas diffusion layer was employed to study the oxygen reduction reaction (ORR) in an operating Anion Exchange Membrane Fuel Cell (AEMFC). The 2D Pt electrode was assembled together with a conventional porous Pt/C counter electrode and an extra Pt/C layer and membrane to reduce the H_2 crossover. Polarization curves at different O_2 partial pressures were recorded and the resulting reproducible ORR activities were normalized with respect to the active surface area (ECSA), obtained by CO stripping. As expected, decreasing the O_2 partial pressure results in a negative shift in open circuit voltage (OCV), cell voltage and maximum attainable current density. For cell voltages above 0.8 V a fairly constant Tafel slope of 60 mV dec^{-1} was recorded but at lower voltages the slope increases rapidly. The observed Tafel slope can be explained by a theoretical model with an associative mechanism where charge- and proton-transfer steps are decoupled, and the proton transfer is the rate-determining step. A reaction order of 1 with respect to O_2 was obtained at 0.65 V which corresponds well with the mechanism suggested above. Based on the obtained catalyst activities, the electrode performance is comparable to good porous electrodes found in the field. The methodology presented in this study is expected to be useful in future kinetic studies of other catalysts for AEMFC.

1. Introduction

The oxygen reduction reaction (ORR) on Pt surfaces in alkaline media has been studied in the past on polycrystalline surfaces [1,2], on difference facets [3,4] and on Pt/C; in KOH and NaOH solutions [5,6] using rotating disk electrode (RDE) experiments and cyclic voltammetry [1,7]. From these studies it is assumed that the ORR kinetics on Pt in alkaline aqueous solutions can be explained as a multi-electron transfer reaction proceeding via two pathways: either a direct reduction of O_2 to OH^- (four-electron pathway) or an indirect reduction of O_2 to H_2O_2 intermediate, which is then reduced to H_2O (two-electron pathway). Regardless of the pathway, the ORR mechanism proceeds through elementary steps. The adsorption of O_2 is believed to occur either by an associative or dissociative mechanism [5,8], but details of the ORR mechanism on real nanoparticle catalysts remain elusive. The following steps (R. 1 to R. 5) describe the direct reduction of O_2 via an associative mechanism where different O-containing intermediates (e.g., MO_2, MO_2H and MOH) are involved [9]. M symbolizes an active site on the surface of the electrocatalyst, while (l) and (g) refer to liquid and gas phases respectively.

$$M + O_{2(g)} \rightleftarrows MO_2 \tag{R.1}$$

$$MO_2 + H_2O_{(l)} + e^- \rightleftarrows MO_2H + OH^- \tag{R.2}$$

$$MO_2H + e^- \rightleftarrows MO + OH^- \tag{R.3}$$

$$MO + H_2O_{(l)} + e^- \rightleftarrows MOH + OH^- \tag{R.4}$$

$$MOH + e^- \rightleftarrows OH^- + M \tag{R.5}$$

In an attempt to better describe this mechanism, Koper [10] suggested to decouple the proton and electron transfer occurring in the second step, R. 2. Such decoupling, described by R. 2a and R. 2b, leads to a pH dependence of the overall reaction rate.

$$MO_2 + e^- \rightleftarrows MO_2^- \tag{R.2a}$$

* Corresponding author.
  E-mail address: emarra@kth.se (E. Marra).

$$MO_2^- + H_2O_{(l)} \rightleftarrows MO_2H + OH^- \tag{R.2b}$$

The ORR rates are conventionally represented by the Tafel equation which expresses the linear relation between electrode potential and the logarithm of the current density [11,12]. Based on RDE experiments, it has been demonstrated that the measured Tafel slope for ORR on Pt changes with applied potential [11,12,13]. Considering the decoupling theory one hypothesis is that this change in Tafel slope accompanies a change in the coverage degree of adsorbed O-containing intermediates [14]. However, the obtained current densities from RDE are convoluted by diffusion limited current densities and therefore the determination of kinetic current densities can involve a significant uncertainty [15]. The RDE approach assumes a total O_2 reaction order of 1 while the potential-dependent coverage degree hypothesis assumes an O_2 reaction order that varies with potential [15,16].

A clear benefit of RDE measurements is the fast evaluation and screening of novel catalysts. However, the conditions in a fuel cell differs from those in RDE and the ORR activities, obtained from RDE experiments [9] are seldom reproduced in experiments using a membrane electrode assembly (MEA) [13,17,18], the heart of the fuel cell. MEA experiments imply that the catalyst interacts with the ionomer in both the electrode and in the membrane, and the supply of O_2 is from the gas phase and not from a saturated aqueous solution as in RDE. These reaction conditions are challenging, and the MEA faces issues related to catalyst degradation [17,19], mass transport [20], temperature, and water management [21,22,23]. As a consequence, the measured ORR activities resulting from RDE studies are usually higher [24,25]. This discrepancy requires a reconsideration of the typical benchmark evaluation of ORR activity [24,26], making MEA studies imperative also in the early stages of catalyst material development.

To make reproducible Pt/C-based catalyst layers with optimal structural properties and composition is rather complex. A simpler approach is to deposit a thin layer of a catalyst onto a gas diffusion layer (GDL) forming a 2D electrode, i.e., to prepare a thin film that can be sandwiched directly with the membrane without adding conducting carbon or ionomer. The thin catalyst layer minimizes the effects of current distribution and mass transport, allowing an easier interpretation of the measured data [27,28]. In comparison with a porous electrode, the less complicated morphology of the thin film electrode makes it easier to measure the electrochemical active surface area (ECSA) without any distortion [29,30]. The 2D electrode can be evaluated with a conventional porous Pt/C electrode at the opposite side of the membrane at typical fuel cell conditions. The much lower catalytic loading on the working electrode compared to the counter electrode also has the advantage that the overpotential of the latter is so small that it can function as a pseudo-reference electrode. This strategy has already been used in proton exchange membrane fuel cells (PEMFCs) for the evaluation of the ORR activity onto layered films of Pt combined with different oxides such as TiO_2 [27], WO_2 [29], Ta_2O_5 [30] and IrO_2 [31]. Another recent example is the investigation of the ORR activity of Pt-rare earth metals (REM) films [32,33].

Alkaline anion exchange membrane fuel cells (AEMFCs) can potentially work with non-precious metal catalysts for the ORR [34]. For instance, Ni electrodes are typically used in classical alkaline water electrolysis [35,36,37]. However, this far, Pt is superior to other catalysts tested in AEMFC, and the current AEMFC technology still suffers from limitations such as limited polymer electrolyte conductivity and poor stability [13,38], inefficient catalyst layer composition [21,39] and complex water management [17,40]. In this study we try for the first time the thin-layer approach in an AEMFC, in order to investigate the ORR kinetics on 2D Pt electrodes. The ORR activity was measured through polarization curves at different O_2 partial pressures. In order to minimize the effect of H_2 crossing over from the hydrogen electrode, being the combined counter and reference electrode, a setup including an extra Pt/C layer between two membranes was employed. In addition to give reproducible results, this configuration allowed to obtain the

ECSA by CO stripping. With this system, the Tafel slope and the reaction order with respect to O_2 were determined and discussed. The methodology presented is expected to be of great use for future kinetic studies of other catalysts for AEMFC.

2. Experimental

2.1. Sputtered thin films of Pt

Thin films of Pt were prepared using a Nordiko 2000 sputter coater with a pure Pt target. The sputtering was performed directly onto a commercial gas diffusion layer (GDL) with a microporous layer (GDL-CT, 410 μm thick). All GDLs were Ar^+-plasma cleaned in situ prior to deposition. The base pressure of the Nordiko 2000 was lower than 1.0×10^{-6} mbar with a working gas pressure of 6.6 mbar under 50 sccm (standard cubic centimeter per minute) of Ar flow. The obtained Pt films on the GDL had a nominal thickness of 3 nm, corresponding to a Pt loading of 6.4 μg cm^{-2}. Initial tests were performed with sputtered Pt films of 20 nm thickness (Pt loading of 42.9 μg cm^{-2}). These thicker Pt layers were fabricated using the same procedure as for Pt 3 nm.

2.2. Double-MEA assembly

A commercial 50 μm thick Aemion™ membrane (Ionomr Innovations Inc.) was cut into two squares of 3 cm^2 each. One of them was sprayed on both sides with an ink composed of Pt/C, ionomer solution (3.78 wt% Aemion ionomer in methanol) and isopropanol. The total solid content was 10 wt% (15% ionomer and 85% Pt/C), giving a Pt loading of 0.4 mg$_{Pt}$ cm^{-2}, with an exposed electrode area of 0.95 cm^2. Before mounting the cell, both membranes (sprayed and non-sprayed) were immersed in 1 M KOH for 24 h (ambient temperature and pressure) to become anion exchanged from iodine (I^-) to hydroxide (OH^-) ions. They were then rinsed with Milli-Q water. In parallel, the sputtered Pt film on GDL was shaped to get a circular gas diffusion electrode (GDE) of 0.95 cm^2.

Fig. 1 shows a schematic representation of the setup with double-MEA consisting of a GDE, a 50 μm Aemion™ membrane and a MEA with sprayed catalyst layers on both sides. In the picture, the GDE is shown to the left and acts as working electrode (WE) while the right-most sprayed catalyst layer acts as a combined counter and reference electrode (CE/RE). To facilitate gas transport, a carbon GDL disk (Sigracet 25BC, 235 μm thick) was added on the counter electrode side. The extra Pt/C layer was included to minimize the effect of H_2 crossover and thus increase the accuracy of the results in the low current-density region as well as the reproducibility of the measurements. The setup
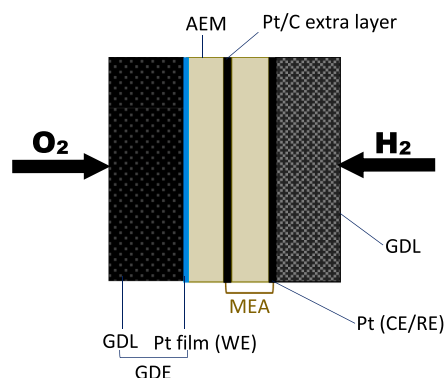

Fig. 1. Schematic of the working electrode (WE) and the combined counter/reference electrode (CE/RE) assembly. An extra Pt/C-membrane layer is introduced between the membrane and the combined CE/RE. O_2 and pure H_2 react in this extra Pt/C layer to form water, reducing the amount of permeating gases. For interpretation of the references to color in this figure legend, the reader is referred to the web version of this article.

with double-MEA was mounted together with commercial PTFE gaskets inside a cell house (Fuel Cell Technologies Inc) using graphite current collectors with customized spiral gas flow channels. With a geometric catalyst area of 0.95 cm^2, the gases had to travel 5.9 cm from the inlet to outlet of the spiral. The cell house was sealed with 5 Nm torque across the bolts. To avoid CO$_2$ contamination, the anion exchange as well as the cell assembling were performed inside a glovebox. As further explained in the next section, the WE was fed with either O$_2$ or Ar, and the CE/RE with either H$_2$ or 5% H$_2$ balanced with Ar. All gases were humidified before entering the fuel cell. The temperature of the cell and humidifiers were set to 30 °C resulting in a relative humidity (RH) of 100% for all the gases. To avoid water condensation in the pipes between the humidifiers and the cell, the temperature of these was adjusted to 34 °C.

2.3. Electrochemical characterization

Electrochemical measurements were performed with a Solartron 1287 potentiostat and a 1255 HF frequency response analyzer. During CO stripping voltammetry, a PAR 273A potentiostat was utilized. All voltages are referred to the Reversible Hydrogen Electrode (RHE).

Before the electrochemical analysis, an activation procedure with potentiostatic steps was performed to reach a steady state. The system was held at 0.5 V and then at 0.2 V, for 10 min each. This sequence was repeated twice. After activation, the electrochemical performance of the WE was obtained by recording polarization curves at four different O$_2$ partial pressures, p$_{O2}$. The used O$_2$ partial pressures were: 100%, 50%, 20% and 10%, and the composition represented dry O$_2$ balanced with Ar. Every polarization curve was recorded stepwise reaching a total number of 14 steps, taking 3 min for each step. It started at the obtained open circuit voltage (OCV) and then the voltage was continuously stepped down to 0.5 V below the OCV value. The first steps close to OCV had a shorter step length while the last steps were separated by 50 mV. By recording 5 points per second, a total of 900 data points were sampled at every step and from them, the last 450 were used to calculate a mean value for obtaining the polarization curves. To get further information about the resistances caused by the polymer membrane and the rate-limiting processes, electrochemical impedance spectroscopy (EIS) was undertaken after every polarization curve. The EIS test was performed galvanostatically at three different DC current densities, -1, -5 and -10 mA cm$_{Pt}^{-2}$. In all cases, the amplitude of the AC perturbation was 5% of the DC current density. The frequency was scanned from 100 kHz to 100 mHz, using 8 steps per decade. During these measurements, O$_2$ and pure H$_2$ (20 sccm on both sides) were fed to the WE and the combined CE/RE, respectively.

In order to determine the ECSA and normalize the results, CO stripping voltammetry was performed. CO stripping in AEMFC is extremely sensitive against any presence of O$_2$, since this oxidant reacts with the CO forming CO$_2$ which in turn, in alkaline environment, forms CO$_3^{2-}$. For this reason, the entire system was flushed with Ar before starting. Due to the lack of established protocols, we adapted the procedure described in a previous PEMFC study to alkaline MEA conditions, at 30 °C and 100% RH [33]:

(I) In order to obtain a blank profile, cyclic voltammetry (5 cycles) was performed between 0.05 and 1 V, at 100 mV s^{-1}. The inlet gas for the WE was pure Ar (100% RH) with a flow rate of 100 sccm, while on the CE/RE, the gas flow was 100 sccm of 5% H$_2$ balanced with Ar. The conditions at the CE/RE were kept throughout the experiment.
(II) By switching gas and feeding the WE channel with dry CO (2% in Ar), a potentiostatic CO adsorption during 5 min at 0.15 V was done.
(III) In order to remove all the remaining CO, the WE was then purged by shifting back to 100 sccm Ar (100% RH) during 34 min.
(IV) The final step was a CO stripping voltammetry, performed in identical conditions as in (I).

Instead of O$_2$, the WE was operated with either CO or Ar, and consequently the double MEA was no longer functional to totally block the crossover of H$_2$. For this reason, 5% H$_2$ balanced in Ar was used at the CE/RE during the measurements. According to Nernst equation, this gives a voltage shift on the CE/WE of 40 mV vs. RHE, so all voltammograms were corrected with this shift.

3. Results and discussion

3.1. Morphological results

The morphology of the GDL, without and with the sputtered thin film of Pt, is shown in the high-resolution scanning electron microscopy (SEM) images in Fig. 2.

As shown in Fig. 2a, the GDL with a microporous layer (MPL) consists of carbon particles of a diameter of up to 50 nm that agglomerate forming a porous structure. After sputter deposition of Pt (Fig. 2b) the macroscopic MPL structure remains unaltered, but the carbon particles appear to be covered with a fine network of Pt nanoparticles, increasing the surface roughness somewhat. Due to the non-directionality of sputtering, Pt will also deposit on the sides of the carbon particles and to some extent coat the inside of the pores. Unlike thin films of the same thickness deposited by using e-beam evaporation [31], DC magnetron sputtering creates smaller Pt crystallites and therefore, as the whole MPL surface is covered with Pt, the contrast difference in the image is low. As described in the experimental section, the coated GDE was sandwiched together with the membrane in order to form a MEA. The non-flat surface structure of the coated MPL implies that only part of the surface, the top particles, are in contact with the membrane and electrochemically active in the cell. The porous structure facilitates the supply of O$_2$ to these areas.

3.2. Electrochemical results

3.2.1. ECSA determination

Hydrogen adsorption and desorption peaks are not very well defined since at low Pt loadings the total charge is dominated by the double layer charging on the carbon substrate, and not by the Pt pseudo-capacitance [41]. Accordingly, it was concluded that these peaks were not sufficient for determining the ECSA. Instead, as it is described in experimental section, CO stripping voltammetry was performed in a similar procedure as previously reported for PEMFC [33]. Fig. 3 shows the CO stripping results, where the blue line represents the blank profile of Pt in humidified inert environment. Despite the efforts to perform completely air-free experiments, the base CV is not perfectly centered around 0 A cm^{-2} indicating some air leakage. During the CO adsorption step at 0.15 V, undertaken between the Pt blank voltammogram and the CO stripping (not shown here), a minor cathodic current was observed when switching from pure Ar to 2% CO in Ar. After 5 min the current stabilized at around 0 mA, indicating a full coverage of CO at the Pt surface.

The CO stripping profile in Fig. 3 is characterized by a faint pre-wave and a broad single CO oxidation peak, centered at ca. 0.73 V$_{RHE}$. If a baseline is drawn from 0 V$_{RHE}$ to the maximum current density obtained at 1 V$_{RHE}$, the ECSA can be calculated from the resulting area below the peak by assuming 420 μC cm$_{Pt}^{-2}$ as the charge required to oxidize the pre-adsorbed CO monolayer. Apparently, the CO adsorption and oxidation are activating or purifying the Pt surface as the PtO reduction peak and the H adsorption peak are more visible in the negative sweep after the stripping. The broad peak indicates that the surface is not preferably oriented in a specific crystallographic plane [42]. The CO electro-oxidation is believed to occur via Langmuir-Hinshelwood mechanism, where the adsorbed CO oxidizes by reacting with the OH generated through partial oxidation of water [43]. Recent investigations have reported that CO shows no mobility during its oxidation in alkaline conditions regardless of the specific structure of Pt, and it is more feasible that OH moves towards the CO [44]. Hence, the CO covering the Pt
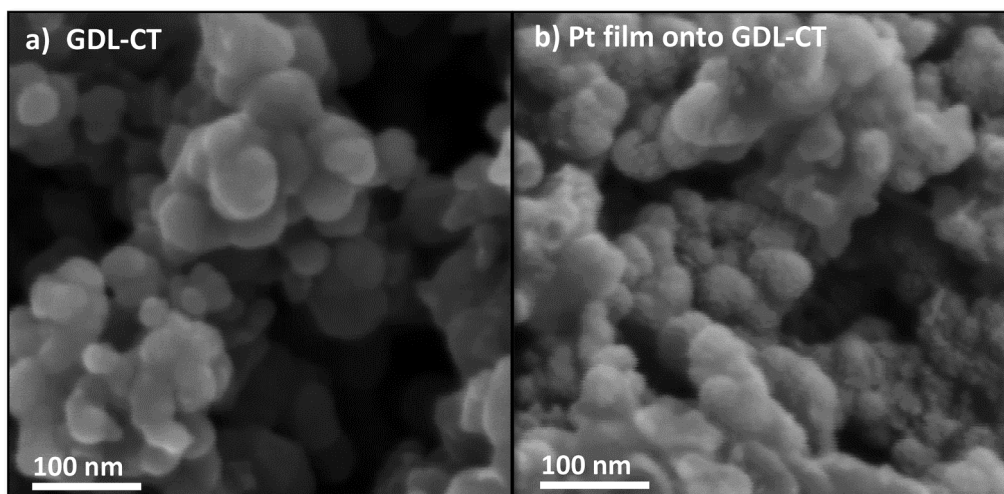
Fig. 2. SEM images of the a) GDL-CT before sputtering and b) with a 3 nm Pt film sputtered on the GDL.
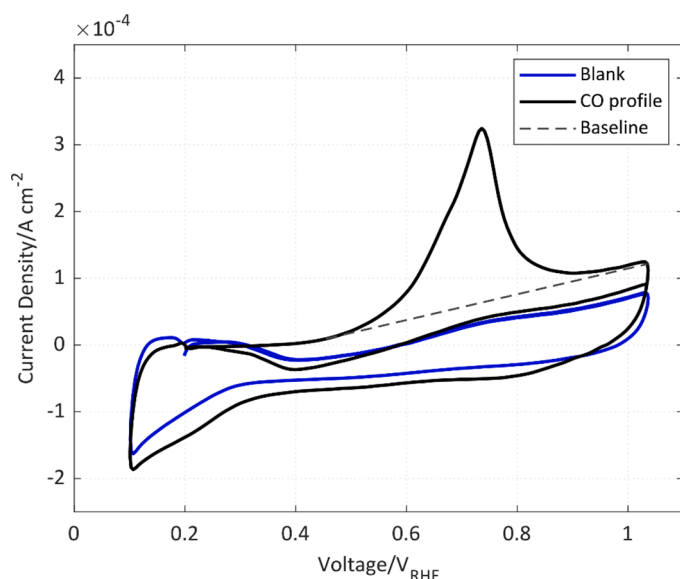

Fig. 3. Blank (blue) and CO profile (black) of the Pt layer. The baseline (dashed gray line) is utilized for calculating the area below the peak. The measurement was performed at 30 °C and 100% RH, with a scan rate of 100 mV s^{-1}. Except during the CO adsorption time, the system worked with Ar (WE) and 5% H$_2$ balanced in Ar (CE/RE). For interpretation of the references to color in this figure legend, the reader is referred to the web version of this article.

particles in direct contact with the membrane will be directly accessible for the electrochemical oxidation while deeper in the electrode the partial oxidation of water and therefore OH formation, first needs to occur. As a consequence, a broader oxidation peak is obtained.

Our CO results differ from those reported by Yang-Neyerlin et al. [45], where the CO profiles from porous Pt, sandwiched with spirocyclic membranes and PtRu as counter electrode, exhibited a highly pronounced pre-wave. By using partial CO stripping experiments in solutions at different pH, Farias et al. [46] reported that the oxidation of a CO adlayer containing a significant number of defects gives rise to the presence of highly distinguishable pre-waves in the stripping voltammograms. The presence of the pre-wave may also depend on other experimental variables such as the surface morphology of the electrode [47,48]. In this context, the network of the Pt nanoparticles gives rise to a non-clear pre-wave and the main peak in Fig. 3 manifests a CO electrooxidation that, initiated on a disordered point, ignited via a

nucleation-growth mechanism [49]. Another important aspect of Yang-Neyerlin's results [45] is that the CO electrooxidation onto porous Pt only succeed when the MEAs had a low H$_2$ crossover. This points out the importance to minimize this effect when performing CO stripping. In this study, by using the setup with double MEA and 5% H$_2$ balanced with Ar at the WE, it was possible to obtain reproducible CO stripping measurements. For instance, the ECSAs for Pt calculated from two different MEAs were 0.83 and 1.00 cm^2. The CO profiles were similar to the one shown in Fig. 3. The ECSA variations are likely due to inherent differences between the samples and also a consequence of the morphological changes at the electrode surface when CO is adsorbed/desorbed [50].

3.2.2. Electrochemical performance at different O$_2$ partial pressures

In order to study ORR activity, polarization curves were recorded at different O$_2$ partial pressures. Fig. 4 displays non-IR corrected steady-state polarization curves, obtained from staircase voltammetry, at four different O$_2$ partial pressures (p$_{O2}$). The first staircases closest to OCV
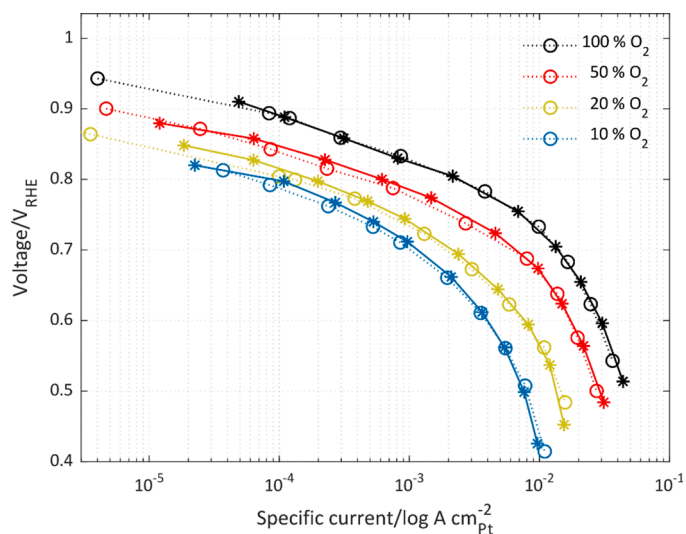

Fig. 4. Steady-state polarization curves at four O$_2$ partial pressures, p$_{O2}$ (100%, 50%, 20% and 10%) in alkaline media, at 30 °C and 100% RH. The setup with double-MEA worked with O$_2$ and H$_2$. The ∗-dotted lines are from one MEA while the o-dotted lines are from a different MEA. The specific currents were normalized with respect to the ECSA estimated by CO stripping. For interpretation of the references to color in this figure legend, the reader is referred to the web version of this article.

were not stable and are therefore excluded from the polarization curves. A repetition of the whole series of polarization curves with a different MEA is also shown in the figure. The current densities were normalized with respect to the ECSA obtained from the CO stripping.

At 30 °C and 100% RH a very high degree of reproducibility was obtained, as exemplified by the duplicated samples shown in Fig. 4. As expected, the polarization curves are shifted downwards with decreasing O_2 partial pressure in accordance with the Nernst shift in the OCV. The fuel cell performance at a given cell voltage increases at higher p_{O2} by increasing the rate of the limiting elementary reactions as well as the OCV [51,52]. Furthermore, independently of p_{O2}, higher voltage losses are seen in the high current density region. Such reduced activity can be caused by limiting surface coverage of intermediates, or a change in the rate determining step at lower cell voltages [16]. However, it is not possible to rule out an effect of local mass transport limitations.

Table 1 shows the specific ORR activities at 0.6 and 0.8 V_{RHE} from one set of the steady-state polarization curves in Fig. 4 (*-dotted lines), extracted via interpolation. At 0.6 V_{RHE} a specific ORR activity of 0.029 A cm_{Pt}^{-2} is obtained for a 6.4 μg_{Pt} cm^{-2} model electrode. If the electrode could be scaled up to have a catalyst loading of 0.4 mg_{Pt} cm_{geo}^{-2}, and a specific area of 50 m_{Pt}^2 g_{Pt}^{-1} (as in commercial Pt catalyst powders [53]) then the performance at 0.6 V_{RHE} would equal 6 A cm_{geo}^{-2}. This shows that the catalyst activity is comparable to good porous electrodes found in the field [17,54,55], but without the extra complications of non-uniform current distribution and mass transport limitations. Therefore, the system is ideal for studying the catalytic activity regardless of the morphology of the porous structure.

Fig. 5 shows the OCV values right before the start of the polarization curves in Fig. 4 (x markers) together with two 100% O_2 OCV values of two MEAs utilized in the beginning of this study (Δ markers). Except for the thickness of the Pt layer (20 nm) and GDL material (Carbel) at the WE, the initial double-MEA is identical to the one shown in Fig. 1. The solid black line is the voltage predicted by Nernst equation (starting from the average of the duplicate samples at 100% O_2). The partial pressures are corrected with respect to the RH. Due to H_2 crossover, a mixed potential is obtained at the electrode [45,56]. As the O_2 partial pressure is decreased, the effect is more pronounced, giving an overall decrease of around 100 mV when lowering the p_{O2} from 100% to 10%, and roughly half of that decrease occurs between 20% and 10%. Even though H_2 crossover still affects the electrode, the double-MEA helps keeping the OCV around 1 V_{RHE}, instead of around 0.9 V_{RHE}, as seen on the double- and single-MEA comparison for Pt 20 nm.

If the extra Pt/C layer in the double-MEA is to be able to oxidize the H_2 crossing from the CE/RE, it also requires O_2 to diffuse from the WE. At a certain p_{O2}, the O_2 and H_2 balance each other in the extra Pt/C layer, and a further reduction of p_{O2} therefore leads to an increase in H_2 crossover. Since going from 20% O_2 to 10% leads to a large drop in OCV, this tipping point is believed to be close to 20% O_2. The H_2 crossover is important to avoid since it causes a mixed potential at the WE, influencing the kinetic evaluation of the ORR activity in the low current density region [28].

3.2.3. Tafel slope

By using central or forward/backward differences, local Tafel slopes for one of the polarization curves with 100% O_2 in Fig. 4 (*-dotted line)

Table 1
Specific ORR activities at 0.6 V_{RHE} ($i_{0.6\ VRHE}$) and 0.8 V_{RHE} ($i_{0.8\ VRHE}$) extracted by interpolation from the steady-state polarization curves in Fig. 4 (*-dotted lines).

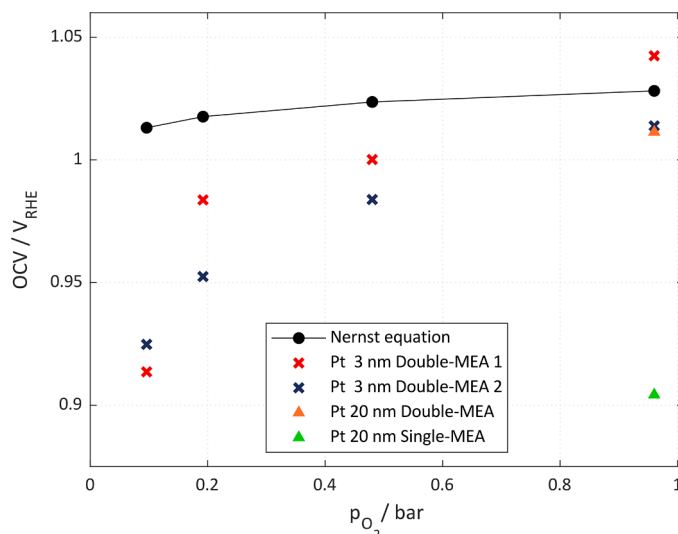| P_{O2}	$i_{0.6\ VRHE}$ [A cm_{Pt}^{-2}]	$i_{0.8\ VRHE}$ [A cm_{Pt}^{-2}]
100%	$2.9 \cdot 10^{-2}$	$2.4 \cdot 10^{-3}$
50%	$1.7 \cdot 10^{-2}$	$6.0 \cdot 10^{-4}$
20%	$7.6 \cdot 10^{-3}$	$1.8 \cdot 10^{-4}$
10%	$4.0 \cdot 10^{-3}$	$9.4 \cdot 10^{-5}$

Fig. 5. OCV values (x) as a function of O_2 partial pressure, performed before every polarization curve in Fig. 4. For comparison, the figure also includes two markers (Δ) that denote the OCV values of two MEAs utilized in the beginning of this study. Regardless the thickness of the Pt layer, all experiments were performed with the setup described in Fig. 1. The solid black line shows the OCV trend predicted by Nernst equation. For interpretation of the references to color in this figure legend, the reader is referred to the web version of this article.

were determined and they are shown in Fig. 6. From the OCV to approximately 0.83 V_{RHE}, the Tafel slope is stable around 60 mV dec^{-1}. For lower O_2 partial pressures (not shown here), the Tafel slope at high potentials is slightly lower, likely due to the H_2 crossover. Below 0.83 V, the slope increases sharply with decreasing voltage for all O_2 partial pressures.

The ORR kinetics on Pt implies a complex multi-electron and proton-transfer process. As we described in the introduction, ORR proceeds in elementary steps and therefore the measured Tafel slope is an apparent value whose variation can occur due to a potential-induced change in the rate-limiting step or the steps before it. In this context, our results fit well with a theoretical description of the ORR kinetics proposed by Shinagawa et al. [14]. In agreement with the decoupling theory mentioned in the introduction (R. 2a and R. 2b), Shinagawa's mechanism decouples the electron and proton transfer step, considering them
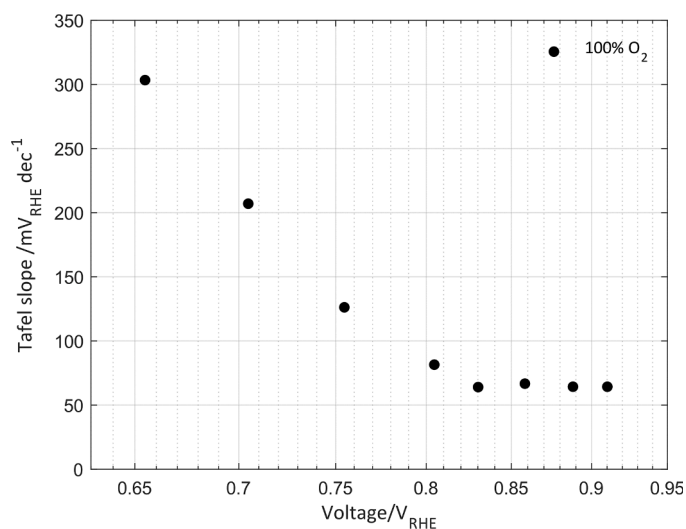

Fig. 6. Local Tafel slopes for one of the polarization curves with 100% O_2 in Fig. 4 (*-dotted line).

as separate steps. This implies the formation of a superoxide ion (MO_2^-), suggested as intermediate by Adzic et al. when studying the ORR in aqueous solution of 0.1 M NaClO$_4$ with NaOH, at pH 11 [57]. Then, by assuming the next proton transfer as the rate-determining step, Shinagawa and coworkers obtained a Tafel slope of 60 mV dec^{-1} in the kinetic region and, as in our experimental results, the slope then increased rapidly at lower voltages. By separating the steps mentioned above, it is assumed that the reaction-rate dependence on the applied voltage originates from a variation in the coverage degree of the O-containing intermediates. The surface-adsorbed species, namely MO_2 in the kinetic region and MO_2^- at lower cell voltages, impact the ORR rate by blocking active surface sites [14]. Eventually, the finite rate of reaction R. 2b leads to chemically limited current density. As a consequence, the rate-limiting step of the ORR in an AEMFC is coverage dependent and hence potential dependent [12,14].

To obtain further insight in the ORR kinetics, electrochemical impedance measurements were performed. However, the extra catalyst layer of the double-MEA caused an inductive behavior and distorted the Nyquist spectra. The data of an EIS test measured at −5 mA cm$_{Pt}^{-2}$ is shown in Fig. S.1 in the supplementary information.

3.2.4. Reaction order with respect to O$_2$

Reaction order, here denoted m, with respect to O$_2$ is defined as the slope of the logarithm of the current density versus the logarithm of O$_2$ partial pressure:

$$m = \left(\frac{\mathrm{d}\log i}{\mathrm{d}\log p_{O_2}} \right)_E \tag{1}$$

By plotting the current density against the p_{O_2} at a fixed voltage on a log-log scale, the reaction order can then be determined [58,59,60]. Fig. 7 shows such a plot at different voltages (0.65, 0.75, 0.80, and 0.85 V$_{RHE}$). The markers represent the current-density values, interpolated from one set of the polarization curves in Fig. 4 ($_*$-lines). The colors represent the same p_{O_2} as in Fig. 4. The dotted lines correspond to the best linear fit at each voltage, and the resulting slopes, m, are presented in Table 2.

Since the efficiency of the double-MEA against crossover decreases at lower p_{O_2}, the current densities at high voltages where the crossover effect is more significant tend to deviate from the linear fitting. For this reason, only potentials below 0.85 V$_{RHE}$ are considered, and above 0.8 V$_{RHE}$ the linear fitting only includes the p_{O_2} for 100 and 50% of O$_2$. At

Table 2
Reaction order, m, with respect to O$_2$ at different voltages (0.85, 0.80, 0.75 and 0.65 V$_{RHE}$). For 0.8 V$_{RHE}$ two slopes are plotted: considering only the two highest p_{O_2}, and when considering all four O$_2$ partial pressures.

E [V$_{RHE}$]	m
Low current density region	
0.85	2.15
Transition region	
0.80	2.00
0.80	1.40
High current density region	
0.75	1.26
0.65	0.97

0.8 V$_{RHE}$, both a line considering all p_{O_2}, and a line considering only 100 and 50% O$_2$, are shown. Table 2 shows the resulting reaction orders, m. In the literature, a first-order dependence on O$_2$ is often seen independent of voltage [15,61,62], while for our measurements in MEA conditions, the apparent reaction order with respect to O$_2$ decreases from 2.15 at 0.85 V$_{RHE}$ to 0.95 at 0.65 V$_{RHE}$. A varying reaction order with voltage can indicate that the rate determining step changes. A reaction order around unity corresponds well with reaction R. 2b as the rate-determining step [7,11], while a reaction order closer to 2 is harder to explain. In RDE measurements, however, the mass-transport limitations affect the measurements at low voltages and therefore a change in the reaction order is not easily observed [15,58].

4. Conclusions

In this study, the ORR activity on Pt was investigated in AEMFC conditions, where a Pt layer deposited onto a GDL forming a 2D electrode was combined with an anion-exchange membrane and a conventional porous Pt/C-electrode at the opposite side. The 2D nature of the working electrode eliminates gas-phase mass-transport effects, making them ideal for studies of catalyst activity and reaction mechanisms. To restrict the influence of H$_2$ crossover and obtain an accurate analysis of ORR, a setup with a double-MEA was used. The polarization curves, obtained from different O$_2$ partial pressures at 30 °C and 100% RH, were reproducible and the ECSA was estimated from CO stripping by calculating the area below a CO oxidation peak centered at around 0.73 V$_{RHE}$. While the geometrical area is equal to 0.95 cm^2, the obtained ECSAs of the two studied MEAs were 0.83 and 1.00 cm^2. Considering the obtained catalyst activities, the electrode performance is comparable to well performing porous electrodes found in the field. As expected, decreasing the O$_2$ partial pressure results in a negative shift in OCV, cell voltage and maximum current density. From the OCV to about 0.8 V$_{RHE}$, the Tafel slope is stable at around 60 mV dec^{-1}, but below that voltage it increases rapidly with decreasing voltage. This variation can be explained in a theoretical model with an associative mechanism where charge- and proton-transfer steps are decoupled, and the proton transfer is the rate-determining step. Unlike what has been shown previously in the literature, the apparent reaction order with respect to O$_2$ decreases from 2 at 0.85 V$_{RHE}$ to 1 at 0.65 V$_{RHE}$, indicating that the rate-determining step changes with voltage, or more likely that crossover and other phenomena affect the catalyst performance.

The extra Pt/C layer in the setup with double-MEA efficiently consumes H$_2$ permeating from the CE/RE as long as there is sufficient O$_2$ present, which in our system seems to be above 20% O$_2$ partial pressure. Nevertheless, the methodology was proven to be of great use for fast screening the intrinsic ORR activity of catalysts at fuel cell conditions. The aim is to use a similar methodology at higher temperatures and with other catalysts in future studies.
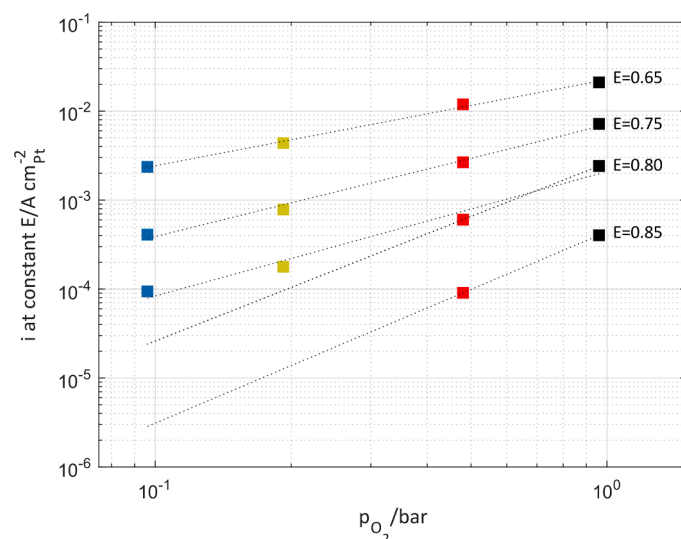

Fig. 7. Current density at fixed cell voltages (0.65, 0.75, 0.80, and 0.85 V$_{RHE}$) plotted against p_{O_2} in a log-log plot. The markers are interpolated from the polarization curves, while the lines correspond to the best linear fit at each voltage. The slope of the lines, m, is shown in Table 2.

CRediT authorship contribution statement

Eva Marra: Investigation, Methodology, Formal analysis, Writing – original draft. **Henrik Grimler:** Formal analysis, Writing – review & editing. **Gerard Montserrat-Sisó:** Resources, Investigation, Writing – review & editing. **Rakel Wreland Lindström:** Supervision, Conceptualization, Writing – review & editing, Funding acquisition. **Björn Wickman:** Supervision, Conceptualization, Writing – review & editing, Funding acquisition. **Göran Lindbergh:** Supervision, Conceptualization, Writing – review & editing, Funding acquisition. **Carina Lagergren:** Supervision, Conceptualization, Writing – review & editing, Funding acquisition.

Declaration of Competing Interest

The authors declare that they have no known competing financial interests or personal relationships that could have appeared to influence the work reported in this paper.

Acknowledgments

Supplementary materials

Supplementary material associated with this article can be found, in the online version, at doi:10.1016/j.electacta.2022.141376.

References

[1] L. Geniès, R. Faure, R. Durand, Electrochemical reduction of oxygen on platinum nanoparticles in alkaline media, Electrochim. Acta 44 (1998), https://doi.org/10.1016/S0013-4686(98)00254-0.

[2] G. Couturier, D.W. Kirk, P.J. Hyde, S. Srinivasan, Electrocatalysis of the hydrogen oxidation and of the oxygen reduction reactions of Pt and some alloys in alkaline medium, Electrochim. Acta 32 (1987), https://doi.org/10.1016/0013-4686(87)90024-7.

[3] C.F. Zinola, A.M. Castro Luna, W.E. Triaca, A.J. Arvia, Kinetics and mechanism of the electrochemical reduction of molecular oxygen on platinum in KOH: influence of preferred crystallographic orientation, J. Appl. Electrochem. 24 (1994), https://doi.org/10.1007/BF00249854.

[4] N.M. Markovic, H.A. Gasteiger, P.N. Ross, Oxygen Reduction on platinum low-index single-crystal surfaces in alkaline solution: rotating ring disk pt(hkl) studies, 1996.

[5] N. Ramaswamy, S. Mukerjee, Fundamental mechanistic understanding of electrocatalysis of oxygen reduction on Pt and Non-Pt surfaces: acid versus alkaline media, Adv. Phys. Chem. 2012 (2012), https://doi.org/10.1155/2012/491604.

[6] W. Jin, H. Du, S. Zheng, H. Xu, Y. Zhang, Comparison of the oxygen reduction reaction between NaOH and KOH solutions on a Pt electrode: the electrolyte-dependent effect, J. Phys. Chem. B 114 (2010), https://doi.org/10.1021/jp102367u.

[7] D.B. Sepa, M.V. Vojnovic, A. Damjanovic, Reaction intermediates as a controlling factor in the kinetics and mechanism of oxygen reduction at platinum electrodes, Electrochim. Acta 26 (1981), https://doi.org/10.1016/0013-4686(81)90037-2.

[8] X. Tian, X.F. Lu, B.Y. Xia, X.W. (David) Lou, Advanced electrocatalysts for the oxygen reduction reaction in energy conversion technologies, Joule 4 (2020) 45–68, https://doi.org/10.1016/j.joule.2019.12.014.

[9] R. Ma, G. Lin, Y. Zhou, Q. Liu, T. Zhang, G. Shan, M. Yang, J. Wang, A review of oxygen reduction mechanisms for metal-free carbon-based electrocatalysts, npj Comput. Mater. 5 (2019), https://doi.org/10.1038/s41524-019-0210-3.

[10] M.T.M. Koper, Theory of multiple proton–electron transfer reactions and its implications for electrocatalysis, Chem. Sci. 4 (2013) 2710, https://doi.org/10.1039/c3sc50205h.

[11] Y.-.H. Fang, Z.-.P. Liu, Tafel Kinetics of Electrocatalytic Reactions: from Experiment to First-Principles, ACS Catal. 4 (2014). https://doi.org/10.1021/cs501312v.

[12] A. Holewinski, S. Linic, Elementary Mechanisms in Electrocatalysis: revisiting the ORR Tafel Slope, J. Electrochem. Soc. 159 (2012) H864–H870, https://doi.org/10.1149/2.022211jes.

[13] L. An, T.S. Zhao (Eds.), Anion Exchange Membrane Fuel Cells, Springer International Publishing, Cham, 2018, https://doi.org/10.1007/978-3-319-71371-7.

[14] T. Shinagawa, A.T. Garcia-Esparza, K. Takanabe, Insight on Tafel slopes from a microkinetic analysis of aqueous electrocatalysis for energy conversion, Sci. Rep. 5 (2015), https://doi.org/10.1038/srep13801.

[15] S. Xu, Y. Kim, D. Higgins, M. Yusuf, T.F. Jaramillo, F.B. Prinz, Building upon the Koutecky-Levich equation for evaluation of next-generation oxygen reduction reaction catalysts, Electrochim. Acta 255 (2017), https://doi.org/10.1016/j.electacta.2017.09.145.

[16] N.P. Subramanian, T.A. Greszler, J. Zhang, W. Gu, R. Makharia, Pt-oxide coverage-dependent oxygen reduction reaction (ORR) kinetics, J. Electrochem. Soc. 159 (2012) B531–B540, https://doi.org/10.1149/2.088205jes.

[17] S. Zaman, L. Huang, A.I. Douka, H. Yang, B. You, B.Y. Xia, Oxygen reduction electrocatalysts toward practical fuel cells: progress and perspectives, Angewandte Chemie Int. Ed. 60 (2021), https://doi.org/10.1002/anie.202016977.

[18] J. Fan, M. Chen, Z. Zhao, Z. Zhang, S. Ye, S. Xu, H. Wang, H. Li, Bridging the gap between highly active oxygen reduction reaction catalysts and effective catalyst layers for proton exchange membrane fuel cells, Nat. Energy 6 (2021), https://doi.org/10.1038/s41560-021-00824-7.

[19] L. Xie, D.W. Kirk, Platinum stability at the cathode of an anion exchange membrane fuel cell, Electrocatalysis 11 (2020), https://doi.org/10.1007/s12678-020-00587-x.

[20] T. Reshetenko, M. Odgaard, D. Schlueter, A. Serov, Analysis of alkaline exchange membrane fuel cells performance at different operating conditions using DC and AC methods, J. Power Sources 375 (2018), https://doi.org/10.1016/j.jpowsour.2017.11.030.

[21] L. Xie, D.W. Kirk, Stability Comparison of Pt and Ni as base metal catalysts in anion exchange membrane fuel cells, J. Electrochem. Soc. 167 (2020), https://doi.org/10.1149/1945-7111/ab8368.

[22] X. Tian, X.F. Lu, B.Y. Xia, X.W. (David) Lou, Advanced electrocatalysts for the oxygen reduction reaction in energy conversion technologies, Joule 4 (2020), https://doi.org/10.1016/j.joule.2019.12.014.

[23] R.W. Lindström, K. Kortsdottir, M. Wesselmark, A. Oyarce, C. Lagergren, G. Lindbergh, Active area determination of porous pt electrodes used in polymer electrolyte fuel cells: temperature and humidity effects, J. Electrochem. Soc. 157 (2010), https://doi.org/10.1149/1.3494220.

[24] W. Chen, Q. Xiang, T. Peng, C. Song, W. Shang, T. Deng, J. Wu, Reconsidering the benchmarking evaluation of catalytic activity in oxygen reduction reaction, IScience. 23 (2020). https://doi.org/10.1016/j.isci.2020.101532.

[25] A. Kongkanand, M.F. Mathias, The priority and challenge of high-power performance of low-platinum proton-exchange membrane fuel cells, J. Phys. Chem. Lett. 7 (2016), https://doi.org/10.1021/acs.jpclett.6b00216.

[26] S. Stariha, K. Artyushkova, M.J. Workman, A. Serov, S. Mckinney, B. Halevi, P. Atanassov, PGM-free Fe-N-C catalysts for oxygen reduction reaction: catalyst layer design, J. Power Sources 326 (2016), https://doi.org/10.1016/j.jpowsour.2016.06.098.

[27] M. Gustavsson, H. Ekström, P. Hanarp, L. Eurenius, G. Lindbergh, E. Olsson, B. Kasemo, Thin film Pt/TiO2 catalysts for the polymer electrolyte fuel cell, J. Power Sources 163 (2007), https://doi.org/10.1016/j.jpowsour.2006.10.005.

[28] H. Ekström, P. Hanarp, M. Gustavsson, E. Fridell, A. Lundblad, G. Lindbergh, A novel approach for measuring catalytic activity of planar model catalysts in the polymer electrolyte fuel cell environment, J. Electrochem. Soc. 153 (2006), https://doi.org/10.1149/1.2170578.

[29] B. Wickman, M. Wesselmark, C. Lagergren, G. Lindbergh, Tungsten oxide in polymer electrolyte fuel cell electrodes—a thin-film model electrode study, Electrochim. Acta 56 (2011), https://doi.org/10.1016/j.electacta.2011.08.046.

[30] M. Wesselmark, B. Wickman, C. Lagergren, G. Lindbergh, Electrochemical performance and stability of thin film electrodes with metal oxides in polymer electrolyte fuel cells, Electrochim. Acta 55 (2010), https://doi.org/10.1016/j.electacta.2009.12.040.

[31] M. Wesselmark, B. Wickman, C. Lagergren, G. Lindbergh, The impact of iridium on the stability of platinum on carbon thin-film model electrodes, Electrochim. Acta 111 (2013), https://doi.org/10.1016/j.electacta.2013.07.108.

[32] B. Eriksson, G. Montserrat-Sisó, R. Brown, T. Skála, R. Wreland Lindström, G. Lindbergh, B. Wickman, C. Lagergren, Enhanced oxygen reduction activity with rare earth metal alloy catalysts in proton exchange membrane fuel cells, Electrochim. Acta 387 (2021), https://doi.org/10.1016/j.electacta.2021.138454.

[33] N. Lindahl, B. Eriksson, H. Grönbeck, R.W. Lindström, G. Lindbergh, C. Lagergren, B. Wickman, Fuel cell measurements with cathode catalysts of sputtered Pt 3 Y thin films, ChemSusChem 11 (2018), https://doi.org/10.1002/cssc.201800023.

[34] D.R. Dekel, Review of cell performance in anion exchange membrane fuel cells, J. Power Sources 375 (2018), https://doi.org/10.1016/j.jpowsour.2017.07.117.

[35] F. Razmjooei, T. Morawietz, E. Taghizadeh, E. Hadjixenophontos, L. Mues, M. Gerle, B.D. Wood, C. Harms, A.S. Gago, S.A. Ansar, K.A. Friedrich, Increasing the performance of an anion-exchange membrane electrolyzer operating in pure water with a nickel-based microporous layer, Joule 5 (2021) 1776–1799, https://doi.org/10.1016/j.joule.2021.05.006.

[36] Y.S. Park, J. Jeong, Y. Noh, M.J. Jang, J. Lee, K.H. Lee, D.C. Lim, M.H. Seo, W. B. Kim, J. Yang, S.M. Choi, Commercial anion exchange membrane water electrolyzer stack through non-precious metal electrocatalysts, Appl. Catal. B 292 (2021), 120170, https://doi.org/10.1016/j.apcatb.2021.120170.

[37] H.A. Miller, K. Bouzek, J. Hnat, S. Loos, C.I. Bernäcker, T. Weißgärber, L. Röntzsch, J. Meier-Haack, Green hydrogen from anion exchange membrane water electrolysis: a review of recent developments in critical materials and operating

conditions, Sustain. Energy Fuels 4 (2020) 2114–2133, https://doi.org/10.1039/C9SE01240K.

[38] T. Novalin, D. Pan, G. Lindbergh, C. Lagergren, P. Jannasch, R.W. Lindström, Electrochemical performance of poly(arylene piperidinium) membranes and ionomers in anion exchange membrane fuel cells, J. Power Sources 507 (2021), 230287, https://doi.org/10.1016/j.jpowsour.2021.230287.

[39] H.A. Firouzjaie, W.E. Mustain, Catalytic advantages, challenges, and priorities in alkaline membrane fuel cells, ACS Catal. 10 (2020), https://doi.org/10.1021/acscatal.9b03892.

[40] B. Zhang, Y. Hua, Z. Gao, Strategies to optimize water management in anion exchange membrane fuel cells, J. Power Sources 525 (2022), 231141, https://doi.org/10.1016/j.jpowsour.2022.231141.

[41] B. Schwanitz, A. Rabis, M. Horisberger, G.G. Scherer, T.J. Schmidt, Sputtered Cathodes for Polymer Electrolyte Fuel Cells: insights into Potentials, Challenges and Limitations, Chimia (Aarau) 66 (2012) 110, https://doi.org/10.2533/chimia.2012.110.

[42] M.J.S. Farias, F.J. Vidal-Iglesias, J. Solla-Gullón, E. Herrero, J.M. Feliu, On the behavior of CO oxidation on shape-controlled Pt nanoparticles in alkaline medium, J. Electroanalytical Chem. 716 (2014) 16–22, https://doi.org/10.1016/j.jelechem.2013.07.017.

[43] I.J. McPherson, P.A. Ash, L. Jones, A. Varambhia, R.M.J. Jacobs, K.A. Vincent, Electrochemical CO oxidation at platinum on carbon studied through analysis of anomalous in situ IR Spectra, J. Phys. Chem. C 121 (2017) 17176–17187, https://doi.org/10.1021/acs.jpcc.7b02166.

[44] M.J.S. Farias, J.J.G. Varela, G.A. Camara, Electrocatalysis of CO oxidation at model Pt surfaces, in: encyclopedia of interfacial chemistry, Elsevier (2018) 489–496, https://doi.org/10.1016/B978-0-12-409547-2.13315-3.

[45] A.C. Yang-Neyerlin, S. Medina, K.M. Meek, D.J. Strasser, C. He, D.M. Knauss, W. E. Mustain, S. Pylypenko, B.S. Pivovar, Editors' choice—examining performance and durability of anion exchange membrane fuel cells with novel spirocyclic anion exchange membranes, J. Electrochem. Soc. 168 (2021), https://doi.org/10.1149/1945-7111/abf77f.

[46] M.J.S. Farias, C. Busó-Rogero, R. Gisbert, E. Herrero, J.M. Feliu, Influence of the CO adsorption environment on its reactivity with (111) terrace sites in stepped Pt electrodes under alkaline media, J. Phys. Chem. C 118 (2014) 1925–1934, https://doi.org/10.1021/jp408975t.

[47] E. Herrero, Q.-.S. Chen, J. Hernández, S.-.G. Sun, J.M. Feliu, Effects of the surface mobility on the oxidation of adsorbed CO on platinum electrodes in alkaline media. The role of the adlayer and surface defects, Phys. Chem. Chem. Phys. 13 (2011) 16762, https://doi.org/10.1039/c1cp21909j.

[48] Y.-.M. Tsou, L. Cao, E. de Castro, Crucial role of low coordination sites in oxygen reduction, CO stripping, and size effect for nano-sized Pt particles, ECS Trans. 13 (2008) 67–84, https://doi.org/10.1149/1.3039766.

[49] R.M. Arán-Ais, F.J. Vidal-Iglesias, M.J.S. Farias, J. Solla-Gullón, V. Montiel, E. Herrero, J.M. Feliu, Understanding CO oxidation reaction on platinum nanoparticles, Journal of Electroanalytical Chemistry. 793 (2017) 126–136. https://doi.org/10.1016/j.jelechem.2016.09.031.

[50] P. Urchaga, S. Baranton, C. Coutanceau, Changes in COchem oxidative stripping activity induced by reconstruction of Pt (111) and (100) surface nanodomains, Electrochim. Acta 92 (2013) 438–445, https://doi.org/10.1016/j.electacta.2013.01.042.

[51] M.M. Mench, in: ed., Fuel Cell Engines, John Wiley & Sons, Inc., Hoboken, NJ, USA, 2008, https://doi.org/10.1002/9780470209769.

[52] J.W. Pratt, J. Brouwer, G.S. Samuelsen, Performance of proton exchange membrane fuel cell at high-altitude conditions, J. Propuls Power 23 (2007), https://doi.org/10.2514/1.20535.

[53] T.R. Garrick, T.E. Moylan, M.K. Carpenter, A. Kongkanand, Editors' choice—electrochemically active surface area measurement of aged Pt alloy catalysts in PEM fuel cells by CO stripping, J. Electrochem. Soc. 164 (2017) F55–F59, https://doi.org/10.1149/2.0381702jes.

[54] H. Adabi, A. Shakouri, N. Ul Hassan, J.R. Varcoe, B. Zulevi, A. Serov, J. R. Regalbuto, W.E. Mustain, High-performing commercial Fe–N–C cathode electrocatalyst for anion-exchange membrane fuel cells, Nat. Energy 6 (2021), https://doi.org/10.1038/s41560-021-00878-7.

[55] H.A. Miller, M.v. Pagliaro, M. Bellini, F. Bartoli, L. Wang, I. Salam, J.R. Varcoe, F. Vizza, Integration of a Pd-CeO $_2$ /C anode with pt and pt-free cathode catalysts in high power density anion exchange membrane fuel cells, ACS Appl. Energy Mater. 3 (2020), https://doi.org/10.1021/acsaem.0c01998.

[56] H. Grimler, A. Carlson, H. Ekström, C. Lagergren, R.W. Lindström, G. Lindbergh, Determination of kinetic parameters for the oxygen reduction reaction on platinum in an AEMFC, J. Electrochem. Soc. 168 (2021), 124501, https://doi.org/10.1149/1945-7111/ac38f8.

[57] M. Shao, P. Liu, R.R. Adzic, Superoxide anion is the intermediate in the oxygen reduction reaction on platinum electrodes, J. Am. Chem. Soc. 128 (2006), https://doi.org/10.1021/ja061246s.

[58] K.C. Neyerlin, W. Gu, J. Jorne, H.A. Gasteiger, Determination of catalyst unique parameters for the oxygen reduction reaction in a PEMFC, J. Electrochem. Soc. 153 (2006), https://doi.org/10.1149/1.2266294.

[59] A. Parthasarathy, S. Srinivasan, A.J. Appleby, C.R. Martin, Pressure dependence of the oxygen reduction reaction at the platinum microelectrode/nafion interface: electrode kinetics and mass transport, J. Electrochem. Soc. 139 (1992), https://doi.org/10.1149/1.2068992.

[60] B.E. Conway, M. Salomon, Electrochemical reaction orders: applications to the hydrogen- and oxygen-evolution reactions, Electrochim. Acta 9 (1964), https://doi.org/10.1016/0013-4686(64)80088-8.

[61] H.A. Hansen, V. Viswanathan, J.K. Nørskov, Unifying kinetic and thermodynamic analysis of 2 e $^-$ and 4 e $^-$ reduction of oxygen on metal surfaces, J. Phys. Chem. C 118 (2014) 6706–6718, https://doi.org/10.1021/jp4100608.

[62] A.M. Gómez-Marín, J.M. Feliu, New insights into the oxygen reduction reaction mechanism on Pt (111): a detailed electrochemical study, ChemSusChem 6 (2013) 1091–1100, https://doi.org/10.1002/cssc.201200847.